Ceramics International 47 (2021) 30729–30740

Contents lists available at ScienceDirect

Ceramics International

journal homepage: www.elsevier.com/locate/ceramint

Nitrogen effects on structure, mechanical and thermal fracture properties of CrN films

Youxing He [a,b], Kewei Gao [a,b], Huisheng Yang [b,**], Xiaolu Pang [a,b,*], Alex A. Volinsky [c]

[a] Beijing Advanced Innovation Center for Materials Genome Engineering, University of Science and Technology Beijing, Beijing, 100083, China
[b] The State Key Laboratory for Advanced Metals and Materials, School of Materials Science and Engineering, University of Science and Technology Beijing, Beijing, 100083, China
[c] Department of Mechanical Engineering, University of South Florida, 4202 E. Fowler Ave., ENG030, Tampa, FL, 33620, USA

ARTICLE INFO

Keywords:
Microstructure
Mechanical properties
Thermal fracture
CrN film

ABSTRACT

In this research, reactive pulsed dc magnetron sputtering with different Ar/N_2 gas flow ratios was used to deposit CrN films with three growth structures on Si substrates. The phase structure, morphology, mechanical properties, thermal fracture properties, and oxidation behavior of films were studied. The surface roughness, residual stress, preferred orientation, and hardness were affected by the gas flow ratio. The film with (200) preferred orientation and zone II structure performed the best. The surface roughness increased to 6 nm with time when the films fractured at 500 °C. The Cr interlayer oxidation caused by oxygen diffusion through grain boundaries and fracture accelerated degradation of CrN films at higher temperatures. A dense microstructure is favorable for preventing coating oxidation.

1. Introduction

Transition metal nitride films have been extensively studied in the last decade due to their excellent abrasive resistance, high hardness, and oxidation resistance, resulting in their use in automotive, aviation, and other applications [1–3]. CrN protective films have low residual stress, a low deposition temperature of 250 °C, and a wide thickness range from a few to dozens of microns, making them suitable for various applications [4,5]. Alloying of anti-oxidation elements into CrN films and the multilayer structures, such as CrN/TiAlN and TiN/CrN, would improve performance compared with single layer nitride [6–9]. A single layer CrN film is still important in the large-scale modern manufacturing industry due to the low cost, simple preparation process and adequate wear resistance [10]. However, the oxidation and thermal failures, such as thermal cracking and delamination would significantly deteriorate the properties of nitride films [11].

The generation of thermal failure is usually ascribed to alternate expansion and contraction of the surface layers of the substrate caused by low thermal conductivity of materials during the cutting or heating process [12–15], which was connected with annihilation of point defects [16]. The large thermal stress and local stress concentration result in crack initiation, where the defects are the preferential sites for crack nucleation, such as the interface between transition layer and substrate [17]. Meanwhile, during the oxidation or high speed dry grinding process in practical application, the atomic transport consists of outward metal diffusion and inward oxygen diffusion through grain boundaries and film cracks, voids and oxide would form at the interface of film [18–20]. Researchers have reported that CrN and TiN were highly oxidized on the surface and underneath of crack caused by change of residual stress during thermal cycle [12,14,21]. Besides, the cracks were initiated and propagated along the oxide layers in the grain boundaries, suggesting that the oxidation-induced thermal failure cracks [22]. Therefore, oxidation has a negative impact on the thermal failure performance, and the two promote each other and jointly play a role in film failure [23–25].

Hence, alloying with antioxidant elements [26] and multilayer films can inhibit the propagation of developed cracks by altering residual stress of films [27,28]. Furthermore, the residual stress and orientation [29] of TiAlN film would affect the origin and extension of film thermal cracking influenced by microstructure with different processing parameters [30–32].The location, propagation and morphology of thermal cracking was influenced by nanocrystal structure and the change of

* Corresponding author. Beijing Advanced Innovation Center for Materials Genome Engineering, University of Science and Technology Beijing, Beijing, 100083, China.
** Corresponding author.
E-mail address: pangxl@mater.ustb.edu.cn (X. Pang).

https://doi.org/10.1016/j.ceramint.2021.07.252
Received 6 May 2021; Received in revised form 24 June 2021; Accepted 27 July 2021
Available online 28 July 2021

Table 1
Chemical composition and mechanical properties of as-deposited CrN films.

Sample	Thickness μm	ratio of chemical component	Residual stress GPa	Surface roughness R_a, nm	Hardness GPa	Elastic modulus GPa
$R_N = 30\%$	1.5	$CrN_{0.91}$	0.21	2.09	21.1 ± 2.4	254.1 ± 11.8
$R_N = 40\%$	1.5	$CrN_{0.94}$	−0.03	0.31	25.5 ± 0.9	272.7 ± 2.5
$R_N = 50\%$	1.3	$CrN_{1.03}$	−0.37	7.96	17.7 ± 0.4	207.1 ± 2.5

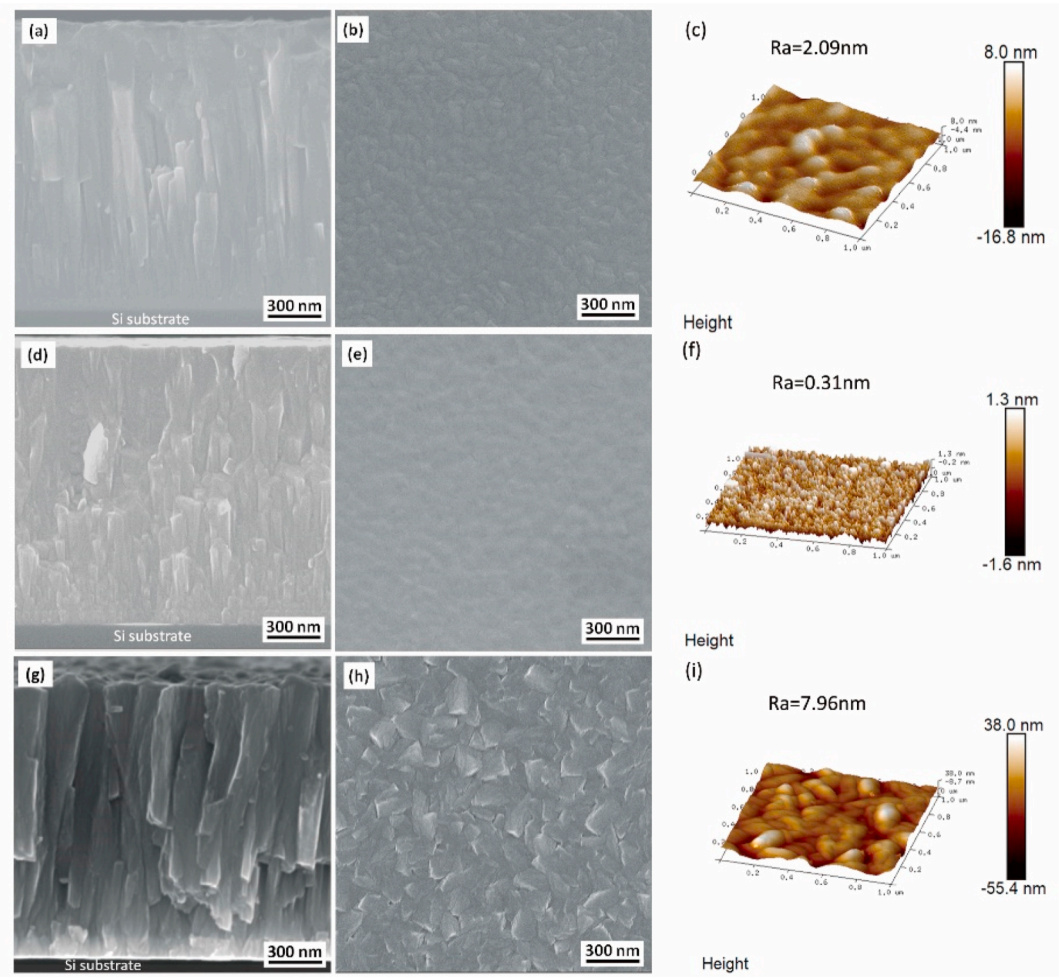

Fig. 1. Cross-section and surface SEM images, and AFM images of CrN films: (a–c) sample ($R_N = 30\%$), (d–f) sample ($R_N = 40\%$), (g–i) sample ($R_N = 50\%$).

residual stress [13,33,34]. However, limited studies aimed at the relationship between microstructure, residual stress and anti-thermal failure for CrN film at high temperature, which is the purpose in this paper.

In this paper, CrN films were prepared by reactive pulsed dc magnetron sputtering on Si (111) substrates by coordinating the duty cycle, power and pulse frequency. Three types of films with diverse microstructures were prepared by altering the Ar and N_2 flow ratio. This research aimed to study the thermal failure, and oxidation resistance of CrN film with diverse microstructures and residual stress. Different thermal behavior was detected during the heating process. These results provide some scientific proof for the application of nitride films at high temperature.

2. Experimental details

The CrN films were deposited on polished Si (111) substrates with original SiO_2 layer by reactive pulsed dc magnetron sputtering (76% duty cycle, frequency of 40 kHz). The purity and diameter of the Cr target were 99.99 wt% and 76.2 mm, and the rotating speed of the sample holder was kept at 20 rpm for the homogeneity of the films. The distance between target and substrate was 7 cm. The Si substrates were cleaned with alcohol for 10 min and then dried. The base pressure was 9.5×10^{-4} Pa, then the polished Si was etched by Ar^+ ions with a bias voltage of −900 V DC for 13 min to clear the surface, and the Cr target was back-sputtered by pulsed DC power of 150 W for 5 min before deposition. A thin Cr transition layer about 110 nm thick was deposited on Si substrate to reduce the residual stress and improve the adhesion between CrN film and Si substrate [35]. The deposition pressure kept at 0.30–0.35Pa. The total deposition time was 3.5 h. The Ar gas flow was fixed at 20sccm, while the N_2 gas flow was 6sccm, 8sccm and 10sccm. The samples are named as sample ($R_N = 30\%$), sample ($R_N = 40\%$) and sample ($R_N = 50\%$) respectively, where the R_N was defined as the gas flow ratio of N_2/Ar.

The surface and cross-section morphology and the CrN film were obtained by scanning electron microscopy (SEM, ZeissEVO-18, ZEISS, Germany). The chemical composition of the surface and cross-section was measured by energy disperse spectroscopy (EDS). The X-ray diffraction (XRD) employing the cos2α sin2ψ method may not be

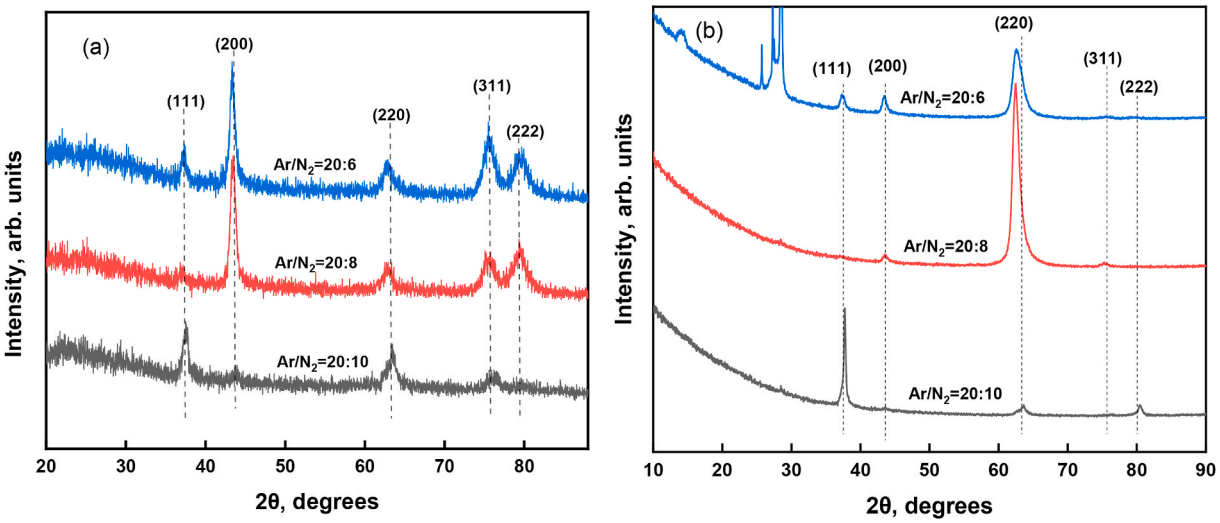

Fig. 2. The xrd scan of samples carry out in (a) GIXRD and (b) Bragg-Brentano setup with different Ar/N_2 flow ratios.

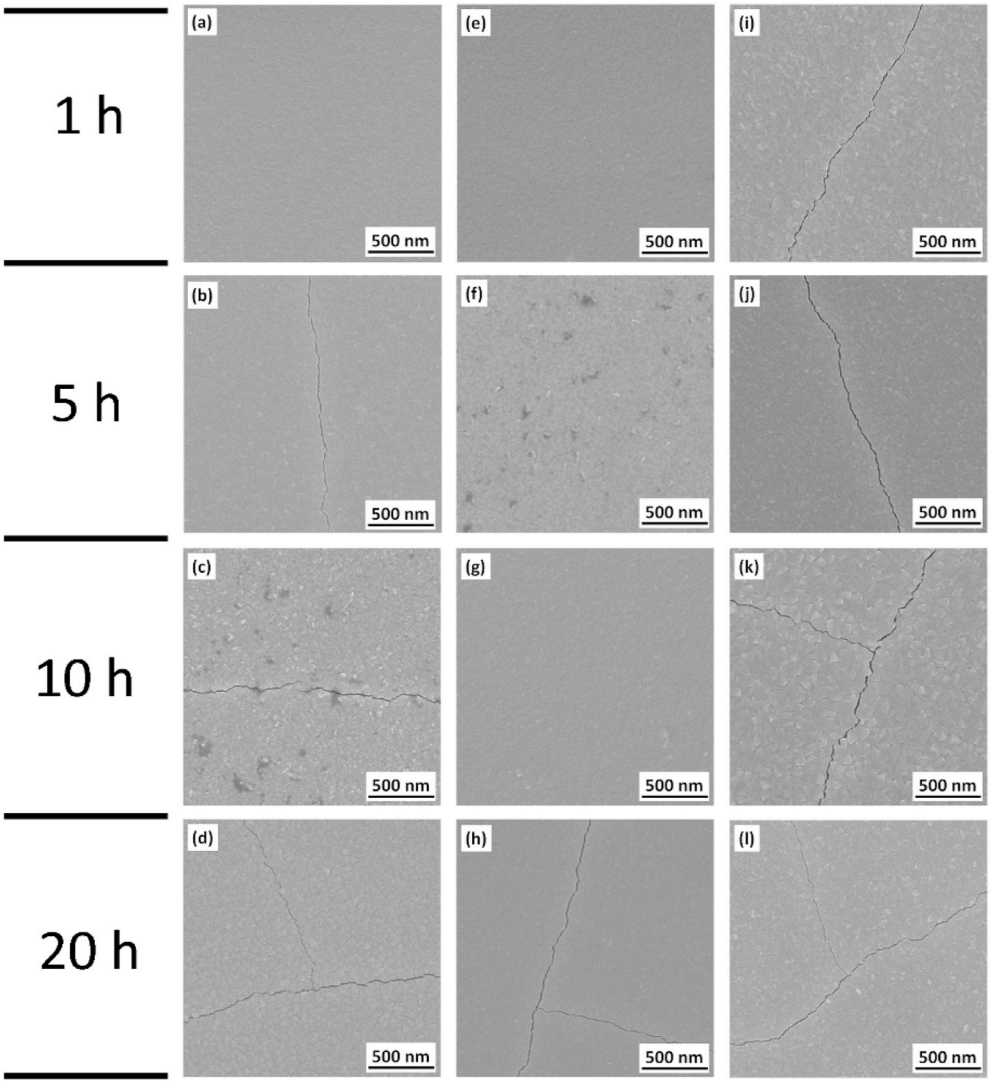

Fig. 3. SEM micrographs of surface changes during oxidation at 500 °C: (a–d) sample (R_N = 30%), (e–h) sample (R_N = 40%), (i–l) sample (R_N = 40%).

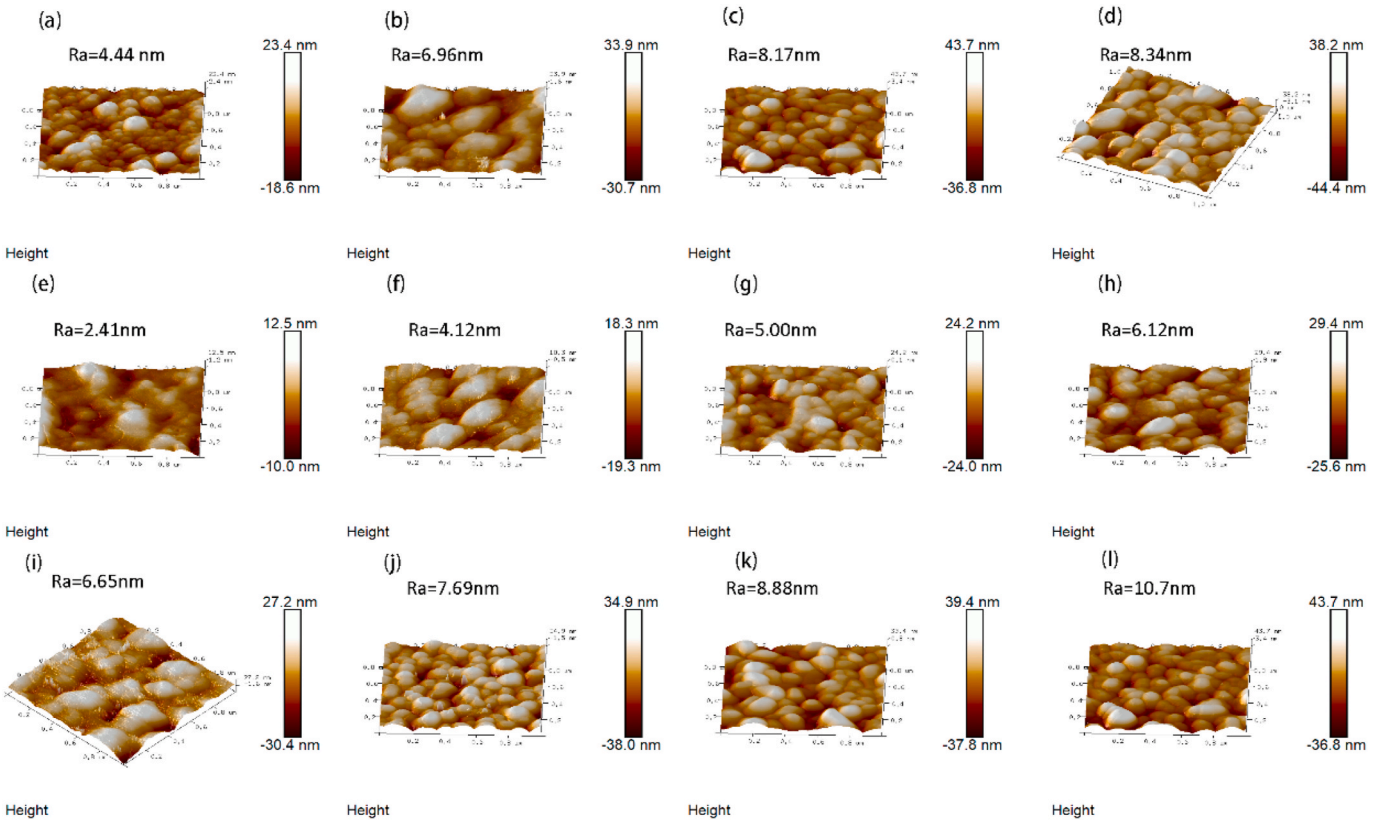

Fig. 4. AMF images of (a–d) sample ($R_N = 30\%$), (e–h) sample ($R_N = 40\%$) and (i–l) sample ($R_N = 50\%$) after oxidation at 500 °C for 1, 5, 10 and 20 h respectively.

appropriate due to the highly textured films [36]. Hence, the change of residual stress, σ_r, of the as-deposited film, was calculated qualitatively from the wafer curvature measurements using Stoney's equation [37]:

$$\sigma_r = \frac{E_s}{6(1-\nu_s)} \frac{t_s}{t_f} \left(\frac{1}{R_f} - \frac{1}{R_s} \right) \quad (1)$$

Here, $E_s \nu_s$, t_s, and t_f are Young's modulus (130 GPa), Poisson's ratio (0.27), the thickness of the substrate, and the CrN films, respectively. R_f and R_s are the radii of the substrate curvature before and after film deposition measured by a profilometer (Dektak, Veeco, USA).

The crystal texture of the CrN films was obtained by grazing incidence X-ray diffraction (XRD, Bruker D8 Advance, Germany) using Cu-Kα irradiation of 40 kV/40 mA. It has been reported that there is a difference between Bragg-Brentano setup and GIXRD setup from the position and intensity of orientation peak [38]. The phase structures of samples after oxidation were measured by GIXRD at an incident angle of 2° to avoid the influence of the substrate while the scan angle range was 10–90° [39].

Cr 2p, N 1s, O 1s, and C 1s core-level XPS spectra were measured by X-ray photoelectron spectroscopy (XPS, Thermofisher ESCALAB 250Xi, USA), using monochromatic Al-Kα radiation with 150 W and 15 kV. To ensure the accuracy of experimental data, the C 1s band energy of 284.8 eV was chosen for charge corrections. The analyzed area was 2.5 × 2.5 mm^2, and the etching depth was based on the SiO_2 thin film reference calibration with 1.1 nm/min etching rate, which was measured using the same etching parameters.

The surface topography and roughness of films were measured by atomic force microscopy (AFM, Dimension Nanoscope V, Veeco Instruments Inc, USA), using NanoScope Analysis software for data processing. A region with 1 μm × 1 μm size was selected for characterization. The background signal was removed to obtain surface roughness and top layer profiles.

The muffle furnace was used for oxidation tests and the oxidation temperature of 500 °C was kept for 1–20 h, reached at a 10 °C/min heating rate. Other oxidation tests at 650 °C, 800 °C and 900 °C were conducted for 1 h, and the samples were air-cooled.

The hardness and reduced elastic modulus were measured by the nanomechanical test system (TI-900 TriboIndenter, Hysitron, USA) with a Berkovich diamond tip at a constant load of 5 mN. The depth of indentation was less than 10% of the film thickness to minimize the substrate effects.

3. Results and discussion

3.1. Microstructure and chemical composition of as-deposited films

Table 1 lists the chemical composition obtained from EDS, and mechanical properties of as-deposited CrN films. Sample ($R_N = 50\%$) has excessive N content, and the atomic ratio of N/Cr is 1.03, while for other samples, N/Cr < 1. Samples ($R_N = 30\%$), ($R_N = 40\%$), and ($R_N = 50\%$) have residual stresses of 0.21 GPa, −0.03 GPa, and −0.37 GPa, respectively. Sample ($R_N = 40\%$) exhibited the highest hardness of 25.5 ± 0.9 GPa and the lowest surface roughness, with the overall film thickness ranging from 1.3 μm to 1.5 μm. The oxygen concentrations for films were kept at 2–3 at% caused by base pressure [40], which has only marginal effect for the purpose of this paper due to the lower concentration [41].

Fig. 1 shows SEM images of the cross-section and surface film microstructure, where all films have a columnar structure. The fine Cr interlayer is about 110 nm thick. Each sample exhibited a unique growth structure model of zones T, I, and II for the top CrN film, respectively. This change was related to the melting point ratio (T/Tm) and deposition parameters [42]. The V-type microstructure of sample ($R_N = 50\%$) seems to be more closely related to "Zone T″ structure, which the formation was attributed to the competitive growth caused by the differences in surface reactivity and diffusivity on differently oriented

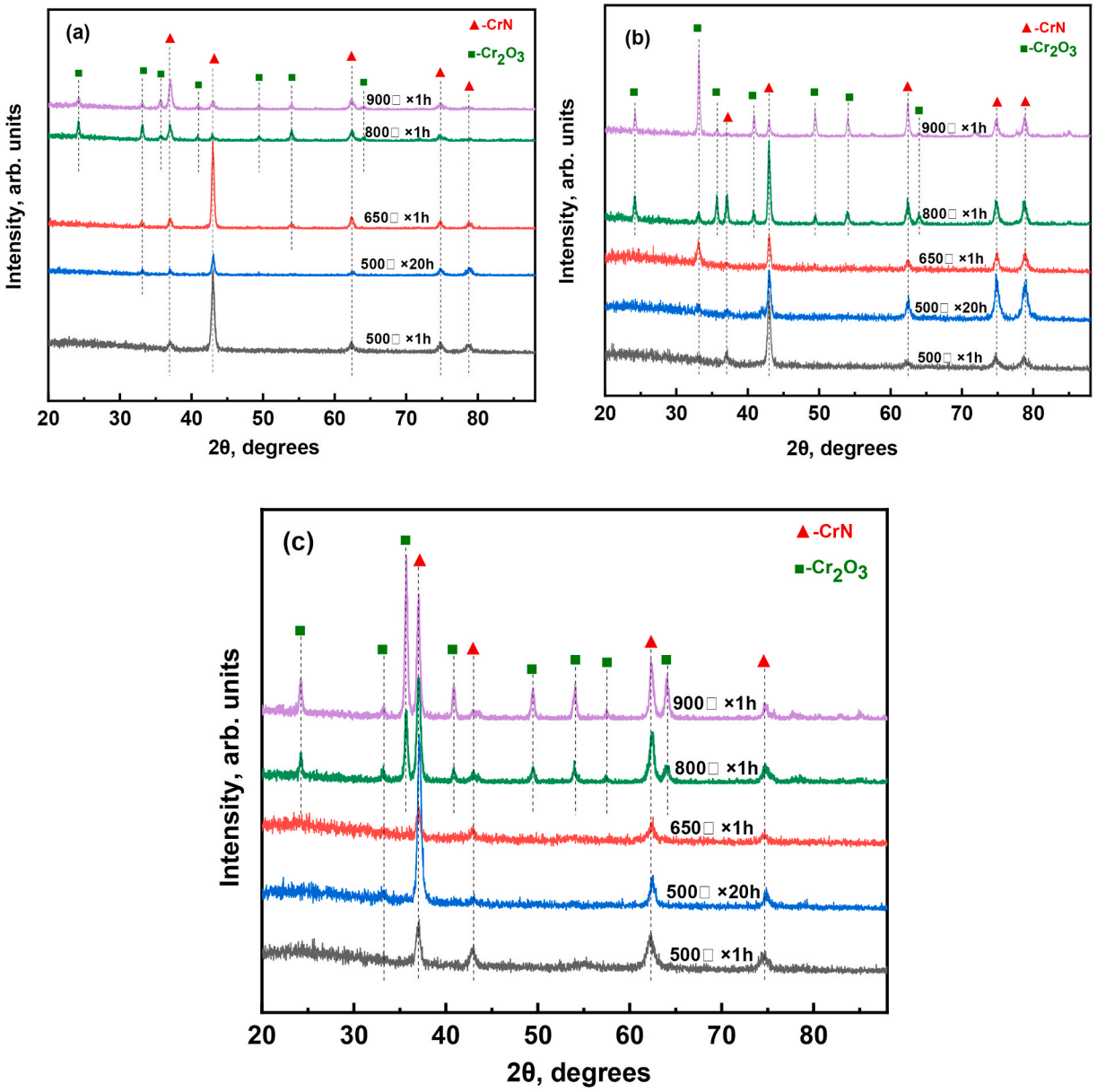

Fig. 5. GIXRD pattern spectra for CrN films after oxidation at different time and temperature: (a) sample ($R_N = 30\%$), (b) sample ($R_N = 40\%$), (c) sample ($R_N = 50\%$).

surfaces structures [43]. There is a visible difference between the samples, where sample ($R_N = 40\%$) has the lowest surface roughness of 0.3 nm and the surface of sample ($R_N = 30\%$) is not flat-like with the R_a of 2 nm, while the morphology of sample ($R_N = 50\%$)is similar to a fish scale. Thus, the CrN films are more compact and thicker under lower N_2 gas flow, as shown in the cross-section images. Sample ($R_N = 40\%$) exhibited a stair-step fracture, whereas others resembled a steep cliff. The film thickness reduced from 1.5 μm to 1.3 μm when the N_2 flow was increased to 10 sccm, attributed to decreased metal adatoms mobility caused by the high nitrogen atom/ion flux [44].

Fig. 2 depicts the grazing incidence X-ray diffraction (GIXRD) patterns of the as-deposited films with different N_2 gas flow. All the curves show a polycrystalline B1–NaCl cubic phase structure, matching the JCPDS card #11–0065 for CrN. The films exhibit (200) preferential orientation under low N_2 gas flow, and there is a shift from (200) to (111) orientation with increased N_2 flow, along with lower (220) and (311) reflections intensity for GIXRD set up. The films exhibit (220) preferential orientation for sample (RN = 30% and 40%) with Bragg-Brentano setup, which was caused by the difference of test principle between GIXRD and Bragg-Brentano set up [38] and the orientation transition during film growth process [30]. The sample ($R_N = 50\%$) exhibits (111) preferential orientation in both models. The grain size was calculated using Debye-Scherrer's formula $D = \frac{K\lambda}{\beta COS\theta}$, where D is the grain diameter, β is the full width at half maximum (FWHM), λ is the wavelength of the incident radiation (Cu Kα = 0.154 nm), θ is the diffraction angle of the CrN (111) reflection. These three films have a similar grain size of 15–19 nm.

The preferred orientation of nitride films is closely related to the microstructure and surface topography. During reactive sputtering, the (111) grain growth orientation is more favored, and the (200) and (200) planes have the lower surface energy [30]. The energy and competitive growth theories have been widely accepted to describe thin film growth. The (200) planes have the lowest surface energy, thus, the texture changes from the initial (200) to (111) as a result of the surface and strain energy competition during growth by GIXRD set up. Researchers have already indicated that the change in orientation is due to the competitive growth theory. Ge et al. proposed the orientation transition induced by the migration of Zr adatoms in ZrN films [45]. As the

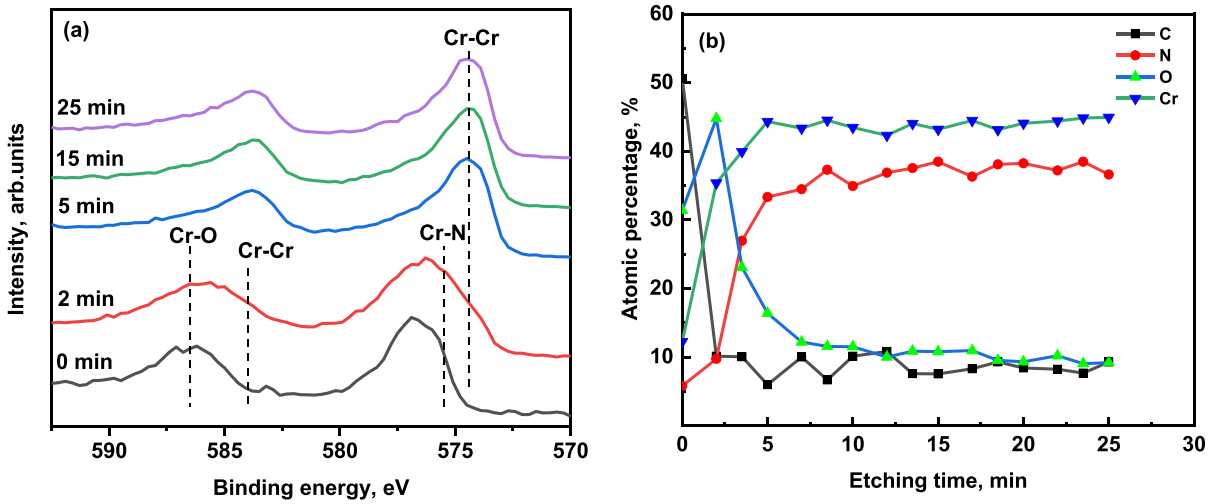

Fig. 6. (a) XPS narrow scan spectra of sample (R_N = 50%) after oxidation at 500 °C for 1 h subjected to various etching time, (b) Atomic percentage of various elements as a function of etching time.

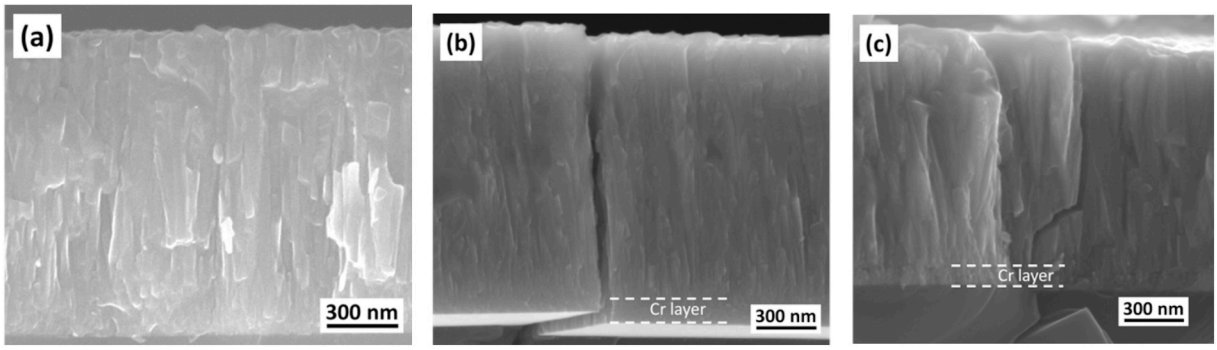

Fig. 7. Cross-section SEM images of: (a) sample (R_N = 30%), (b) sample (R_N = 40%) and (c) sample (R_N = 50%) after oxidation at 500 °C for 20 h.

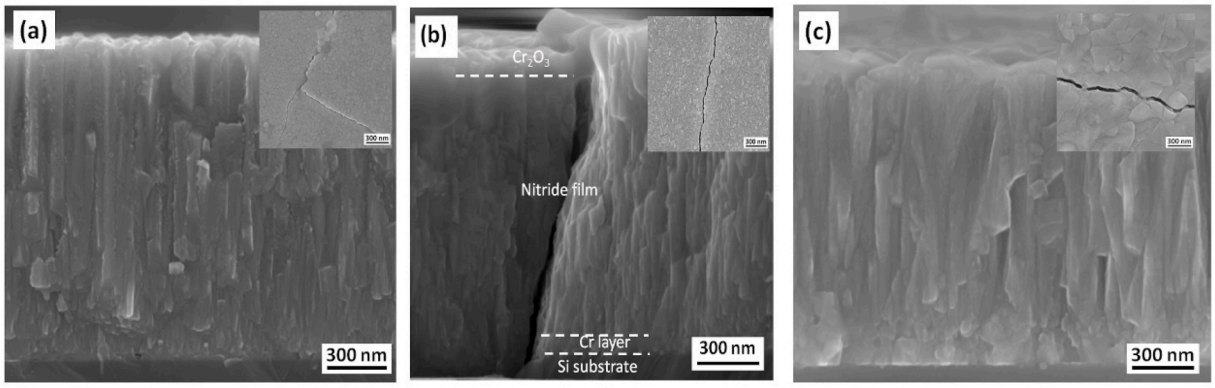

Fig. 8. Cross-section SEM images of: (a) sample (R_N = 50%), (b) sample (R_N = 40%) and (b) sample (R_N = 50%) oxidized at 650 °C for 1 h.

intensity of (111) orientation gradually decreases by changing N_2 flow due to change in N vacancies formation energy, the ZrN films become more compact and have lower surface roughness [46,47]. Also, temperature and bias voltage control the kinetic energy of the impinging ions. 3D kinetic Monte Carlo modeling of stoichiometric TiN indicates the predominance of thermally activated surface diffusion events, structure, and surface roughness controlled by altering the collision parameter/interaction distance based on the modified sputtering model [48]. Furthermore, the formation of mounded surfaces and roughness in epitaxial growth is closely related to the Ehrlich-Schwoebel barriers affected by temperature [49]. Nitride films, specifically 4–6 groups nitrides, such as CrN and VN, have a complex structure caused by the metal/N atomic ratio, where point defects affect the texture, mechanical and thermal properties [50]. Calamba et al. indicated that the N vacancy would increase the strain and defects with the nitrogen tendency to stick to Al, finally distorting the growth process of $TiAlN_y$ films [51]. Furthermore, le Febvrier et al. have reported a p-type conduction of nitrogen-rich CrN combined with aluminum doping, where the film exhibited excellent thermoelectric properties [52]. In the complex magnetron sputtering process, the energy or competitive growth

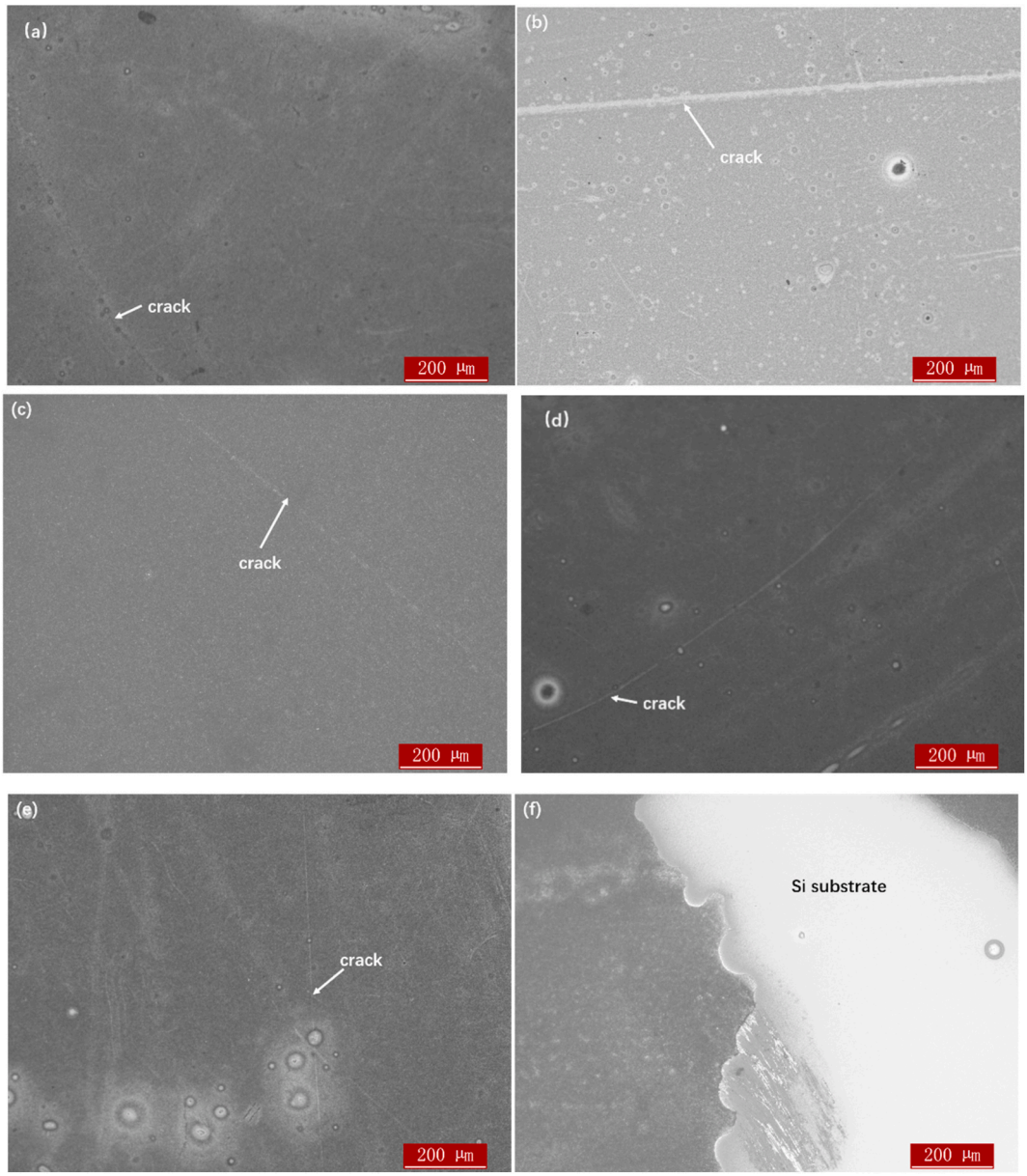

Fig. 9. Optical microscope surface images of (a,c,e) sample (R_N = 30%,40%,50%, respectively) oxidation at 800 for 1 h; (b, d, f) sample (R_N = 30%,40%,50%, respectively) oxidation at 900 for 1 h.

theories could not explain these phenomena thoroughly.

Table 1 lists the residual stress of as-deposited films, where sample (R_N = 30%) has tensile stress (0.21 GPa), while samples (R_N = 40%) and (R_N = 50%) have compressive stress. However, residual stress changes from compressive to tensile stress with film thickness [53]. Jamnig et al. observed that compressive stress was suppressed by a faster deposition rate [54]. In this case, residual stress in films primarily consisted of the inherent stress caused by defects, lattice distortions and the thermal stress caused by the difference in thermal expansion coefficients between the film and substrate, which depend on temperature [55,56]. However, the difference in thermal stress is insignificant, as all the films are deposited at the same temperature. Nitrogen and metal vacancies caused by different Ar/N_2 flow ratio were found in the sub-stoichiometric sample (R_N = 30% and 40%) and over-stoichiometric sample (R_N = 50%) films. Hence, the residual stress was significantly influenced due to the change of volume fraction of grain boundaries and film texture caused by varying intensity and energy of the incident particle flux [50]. Furthermore, the difference of residual stress between sample (R_N = 40%) and sample (R_N = 40%) was attributed to the gradient columnar structure [30].

3.2. Oxidation behavior under various conditions

Figs. 3–4 present the surface changes of three different CrN films after 1–20 h of oxidation at 500 °C. Cracks appear on all film surfaces at different times, with samples C and B being the first and last ones to fracture, respectively. Surface roughness increased with time for samples shown in Fig. 4. The roughness was about 6 nm when the first cracks appeared in all films. Cracks and film fractures are inevitable during the heating process, as the residual stress transformed from compressive to tensile state [34,55,57].

Fig. 5 depicts GIXRD patterns of films oxidized at various time and temperature. Diffraction reflections from different orientations of the CrN phase are retained for samples (R_N = 30%) and (R_N = 40%) with ense columnar structure (Fig. 5(a, b)). After oxidation at 500 °C for 20 h and 650 °C for 1 h, diffraction reflections associated with the Cr_2O_3

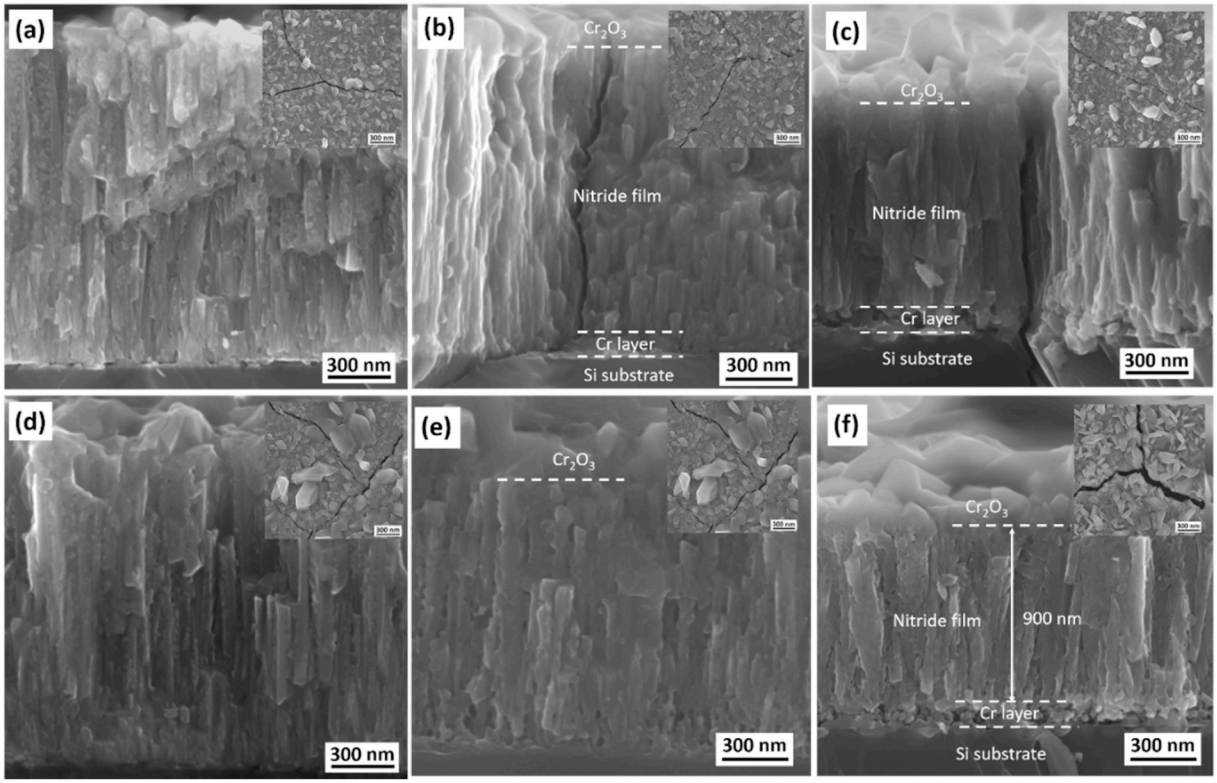

Fig. 10. Cross-section SEM images of (a, d) sample (R_N = 30%), (b, e) sample (R_N = 40%) and (c, f) sample (R_N = 50%) after oxidation at (a, b, c) 800 °C and (d, e, f) 900 °C for 1 h.

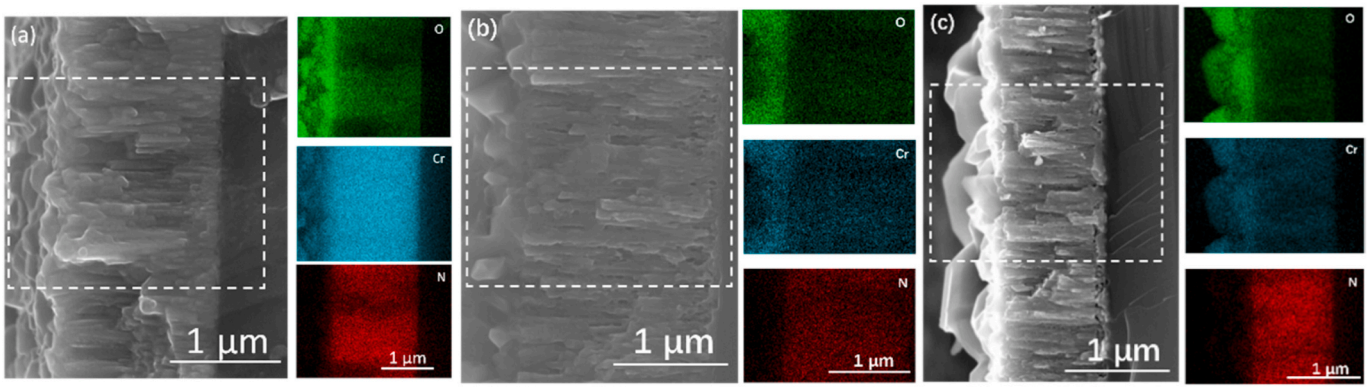

Fig. 11. Cross section scanning maps of samples oxidation at 900 °C for 1 h, (a) sample (R_N = 30%), (b) sample (R_N = 40%) and (c) sample (R_N = 50%).

Table 2
Chemical composition of CrN films after oxidation at various temperatures.

Oxidation temperature °C	Atomic percentage of elements, %								
	Sample (R_N = 30%)			Sample (R_N = 40%)			Sample (R_N = 50%)		
	Cr	N	O	Cr	N	O	Cr	N	O
650	50	36	14	50	36	14	50	39	11
800	47	26	27	47	23	30	46	22	32
900	44	7	49	45	12	43	45	15	40

phase (JCPDS 38–1479) are observed, while those are weaker for sample (R_N = 50%). However, the Cr_2N and Cr reflections are not distinct here due to the low temperature and short oxidation time. The Cr_2O_3 diffraction reflections are present at 800 °C and 900 °C.

Fig. 6 presents the Cr 2P core level spectra obtained from the sample (R_N = 50%) oxidized at 500 °C for 1 h, as a function of sputtering time to obtain more accurate information regarding the phase changes in the film during oxidation. Before etching, the peak at ~576 eV can be deconvoluted into two peaks related to the Cr 2p3/2 electrons: nitride at ~575.5 eV and oxide at ~577 eV in the 570–592.5 eV binding energy

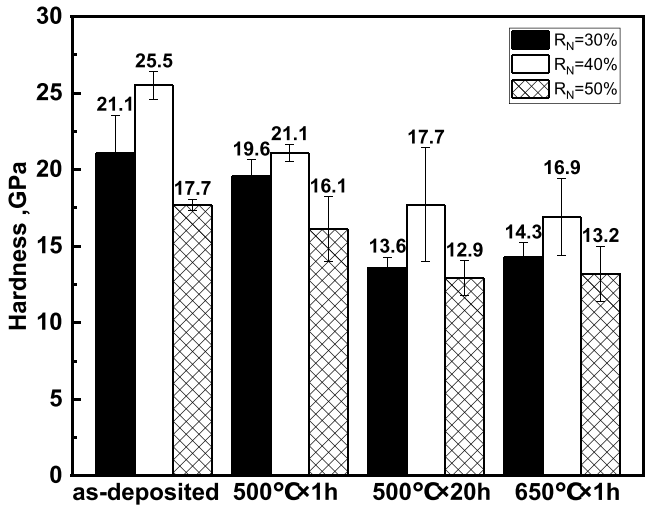

Fig. 12. Hardness of the samples subjected to various oxidation conditions.

range of Cr 2p 3/2 spin-split components in the Cr 2p spectra. Then the Cr peak shifts to 574.4 eV for Cr–Cr after etching for 5 min [58]. Cortazar-Martínez et al. found that the metallic state coexists with the oxide states along the probing depth of XPS, including the top surface during chromium oxidation [59]. The Cr–Cr bond appeared afterward and continued until the end of the sputtering process, with the atomic percentages of the profile shown in Fig. 6(b). The decomposition of nitride films into Cr and Cr_2N is slow but inevitable at 650 °C due to the lower mobility of O atoms at lower temperatures, which is generally drastic over 900 °C [57]. Hence, after oxidation at 500 °C, the possible reactions for CrN are [20]:

$$4CrN \rightarrow 2Cr_2N + N_2 \quad (1a)$$

$$4CrN+3O_2 \rightarrow 2Cr_2O_3+N_2 \quad (2)$$

$$2Cr_2N \rightarrow 4Cr + N_2 \quad (3)$$

$$2Cr_2N+3O_2 \rightarrow 2Cr_2O_3+N_2 \quad (4)$$

$$4Cr+3O_2 \rightarrow 2Cr_2O_3 \quad (5)$$

For TiN, Ti out-diffusion during oxidation leads to a collapse of the nitrogen octahedron, making neighboring Ti bonds weaker and allowing these Ti atoms to diffuse out. N atoms would form N_2 stored in the film, thus, the pressure caused by N_2 would eventually cause TiO_2 surface rupture [60]. Oxidation of Cr leads to a large volume expansion, and the adhesion between the Cr_2O_3 and unoxidized film is insufficient to keep the oxide layer intact [18]. Fig. 6 showed that the oxide was about few nanometers thick, and since the impact of oxide layer on thermal failure can be negligible, the relaxation of residual stress during high temperature was the main reason for the film with zone T [17]. Furthermore, the oxidation rate is not uniform as surface undulations would promote local stress concentrations and fracture the film [56]. The mechanical cracks of the oxide layer were closed related to the change of stress during oxide growth process. Stress accumulation during thin film zirconium oxide growth was observed, which would promote local stress concentrations and fracture the oxide film [61]. Thus, the film with zone II would form a dense protective oxide layer and have higher resistance to cracks due to the gradient structure with lower residual stress and surface roughness. Therefore, the lower surface roughness reduces the occurrence of regions with concentrated local stress in the early oxidation stage that corresponds with Fig. 4 [18].

In Fig. 3 cracks appear at different times during the oxidation process, particularly in samples (R_N = 40%) and (R_N = 50%) with a disparate growth model. Fig. 7 shows a cross-section SEM image of sample (R_N = 40%) after oxidation at 500 °C for 20 h. Fig. 7(b) presents dense columnar crystals below the subsurface, while the columnar structure near the surface becomes indistinct. In contrast, the interface between the Cr layer and nitride has some changes in sample (R_N = 50%) compared with the as-deposited film.

In order to explore the influence caused by cracks, the films were heated to 650 °C, 800 °C and 900 °C for 1 h to accelerate the oxidation

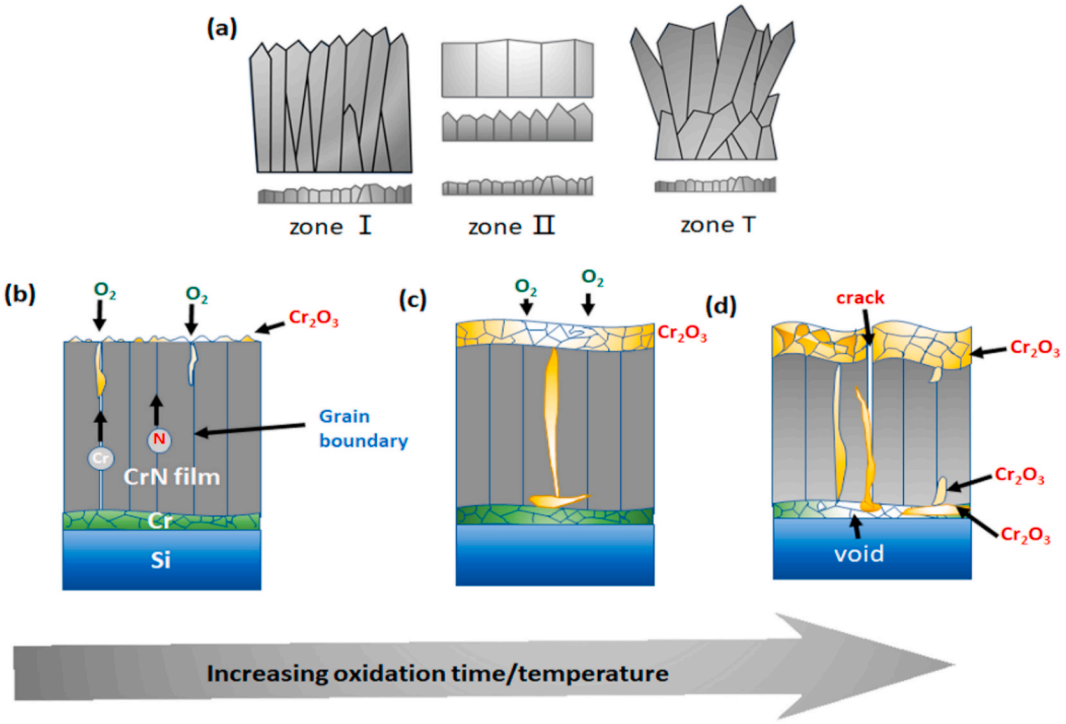

Fig. 13. Schematic of the oxidation process: (a) as-deposited film growth model, (b–d) oxidation process with the increase of time/temperature.

process. The film is fractured, as shown in Fig. 8(a–c); however, no obvious separation between the film and the substrate was detected at 650 °C, although some particles were distributed on the grain boundaries in sample (R_N = 30%). The breakage and desquamation were obviously detected by optical microscope for sample (RN = 50%) in Fig. 9. At 800 °C, the Cr layer in samples (R_N = 30%) and (R_N = 50%) disappeared instead of forming particles and voids. For sample (R_N = 30%), oxidation at grain boundaries was more serious, as shown in Fig. 10 and the difference in the TEC between the oxide and nitride promoted cracking and oxidation [55]. The Cr layer is still closely integrated with nitride and substrate of sample (R_N = 40%). The oxidation activation energy for dense coatings is higher than loose columnar coatings, which confirms their better protective properties during oxidation [62]. The Cr layer was consumed for all films and local delamination occurred between Cr layer and nitride for the sample (RN = 50%) in Fig. 10, which corresponded to Fig. 9. The oxygen diffused from the cracks and further spread along the film-substrate all around and subsequently attacked coating materials, which promote the oxidation of Cr and the spread of delamination at film-substrate interface [63]. Furthermore, the interlayer Cr would further react with Si substrate and form granular Chromium-silicon and oxygen compounds [64]. With the temperature increase to 900 °C, the interface between oxide layer and residual nitride film was obvious, as shown in Fig. 11.

Table 2 lists the chemical composition of films oxidized at different conditions. The decomposition of nitride is slow at low temperature, whereas oxygen concentration rises rapidly from 13.8% to 49% with temperature. Oxygen diffused through the oxide layer and covered the film completely, as shown in Fig. 13.

The hardness of as-deposited films is grouped for nitride films deposited by magnetron sputtering, as shown in Fig. 12. The Hall-Petch theory could explain the hardness of the original films with compressive stress based on the grain size, while dense and tight columns also contributed to increased hardness [46,65]. The mechanical properties of the group 4–6 nitride films, such as MoN, WN_x, are different between non-stoichiometric and stoichiometric configurations, usually attributed to the higher crystalline quality and/or lower N content [66,67]. Sangiovanni et al. indicated that $VN_{0.8}$ has higher elastic shear stiffness than VN, which means that anion vacancies induce hardening demonstrated by first-principles calculations. The $V_{0.5}Mo_{0.5}N_x$ film hardness increased with nitrogen vacancy concentration, due to a combination of dislocation pinning at point defect sites and the strengthening of metal–N, p (N)–deg (Me) bonds [68]. The group b-d is the hardness after oxidation at 500 °C for 1 h and 20 h, and at 650 °C for 1 h, respectively. The hardness is reduced with time and temperature, however, sample (R_N = 40%) has the highest hardness either before or after oxidation, which is reduced from 25.5 ± 0.9 GPa (as-deposited) and 17.7 ± 3.7 GPa (500 °C, 20 h) to 16.9 ± 2.5 GPa (650 °C, 1 h). This decrease is attributed to fewer defects and lattice distortions induced by the sputtering process and grain growth. The surface roughness was high in the films oxidized at 800 °C and 900 °C.

The structure affects the fracture resistance and mechanical properties during oxidation at various conditions. As cracks appear, the interlayer would oxidize soon before the nitride film, leading to the failure of film at 800 °C and higher.

4. Conclusions

In this research, the CrN films with zones T, I, and II growth were obtained by altering the Ar/N_2 gas flow ratio. The sputtering gas ratio could affect surface morphology, roughness, and deposition rate. The film thickness decreased from 1.5 μm to 1.3 μm with increased N_2 flow. The XRD patterns showed that the preferred orientation had shifted from (200) to (111) in the presence of high N_2 flow. Meanwhile, the residual stress changed from compressive to tensile with film thickness, and the CrN_x films ($x < 1$) exhibited higher hardness due to refined grains and anion vacancies.

Cracking is inevitable during the oxidation process, however, CrN film with zone II growth has a high resistance to thermal cracking during oxidation at 500 °C due to lower residual stress, roughness, and dense columnar structure, and decreases the rate of oxygen diffusion. These films also exhibited higher hardness after oxidation at 500 °C or 650 °C.

The oxide layer expanded and fractured faster as the temperature was elevated to 800 °C and higher. The interface between the film and substrate was destroyed due to diffused oxygen along the grain boundaries and cracked rapidly. The Cr interlayer was almost completely exhausted instead of forming voids and oxide particles. The microstructure of CrN coatings is the key critical characteristic for oxidation, the dense coating exhibited excellent oxidation resistance and mechanical properties.

Declaration of competing interest

The authors declare that they have no known competing financial interests or personal relationships that could have appeared to influence the work reported in this paper.

Acknowledgments

This research was supported by the National Natural Science Foundation of China (No. 51922002 and 51771025), the Fundamental Research Funds for the Central Universities (No. FRF-TP-17-19-003C1Z). AV acknowledges support from the Government of the Russian Federation (proposal No. 2020-220-08-6662).

References

[1] P.S. Souza, A.J. Santos, M.A.P. Cotrim, A.M. Abrão, M.A. Câmara, Analysis of the surface energy interactions in the tribological behavior of ALCrN and TIAlN coatings, Tribol. Int. 146 (2020), https://doi.org/10.1016/j.triboint.2020.106206.
[2] A. Singh, S. Ghosh, S. Aravindan, Investigation of oxidation behaviour of AlCrN and AlTiN coatings deposited by arc enhanced HIPIMS technique, Appl. Surf. Sci. 508 (2020), https://doi.org/10.1016/j.apsusc.2019.144812.
[3] O. Çomakli, Influence of CrN, TiAlN monolayers and TiAlN/CrN multilayer ceramic films on structural, mechanical and tribological behavior of β-type Ti45Nb alloys, Ceram. Int. 46 (2020) 8185–8191, https://doi.org/10.1016/j.ceramint.2019.12.046.
[4] B. Navinsek, P. Panjan, I. Milosev, Industrial applications of CrN (PVD) coatings, deposited at high and low temperatures, Surf. Coating. Technol. 97 (1997) 182–191, https://doi.org/10.1016/S0257-8972(97)00393-9.
[5] R. Elo, S. Jacobson, T. Kubart, Tailoring residual stresses in CrNx films on alumina and silicon deposited by high-power impulse magnetron sputtering, Surf. Coating. Technol. 397 (2020), https://doi.org/10.1016/j.surfcoat.2020.125990. ARTN 125990.
[6] O. Comakli, Influence of CrN, TiAlN monolayers and TiAlN/CrN multilayer ceramic films on structural, mechanical and tribological behavior of beta-type Ti45Nb alloys, Ceram. Int. 46 (2020) 8185–8191, https://doi.org/10.1016/j.ceramint.2019.12.046.
[7] F.L. Ma, J.L. Li, Z.X. Zeng, Y.M. Gao, Structural, mechanical and tribocorrosion behaviour in artificial seawater of CrN/AlN nano-multilayer coatings on F690 steel substrates, Appl. Surf. Sci. 428 (2018) 404–414, https://doi.org/10.1016/j.apsusc.2017.09.166.
[8] Y.X. Ou, J. Lin, H.L. Che, W.D. Sproul, J.J. Moore, M.K. Lei, Mechanical and tribological properties of CrN/TiN multilayer coatings deposited by pulsed dc magnetron sputtering, Surf. Coating. Technol. 276 (2015) 152–159, https://doi.org/10.1016/j.surfcoat.2015.06.064.
[9] H.C. Barshilia, M. Ghosh, Shashidhara, R. Ramakrishna, K.S. Rajam, Deposition and characterization of TiAlSiN nanocomposite coatings prepared by reactive pulsed direct current unbalanced magnetron sputtering, Appl. Surf. Sci. 256 (2010) 6420–6426, https://doi.org/10.1016/j.apsusc.2010.04.028.
[10] R. Ferreira, O. Carvalho, L. Sobral, S. Carvalho, F. Silva, Influence of morphology and microstructure on the tribological behavior of arc deposited CrN coatings for the automotive industry, Surf. Coating. Technol. 397 (2020), https://doi.org/10.1016/j.surfcoat.2020.126047. ARTN 126047.
[11] T. Guo, J.Y. He, X.L. Pang, A.A. Volinsky, Y.J. Su, L.J. Qiao, High temperature brittle film adhesion measured from annealing-induced circular blisters, Acta Mater. 138 (2017) 1–9, https://doi.org/10.1016/j.actamat.2017.07.026.
[12] C. Kirchlechner, K.J. Martinschitz, R. Daniel, M. Klaus, C. Genzel, C. Mitterer, J. Keckes, Residual stresses and thermal fatigue in CrN hard coatings characterized by high-temperature synchrotron X-ray diffraction, Thin Solid Films 518 (2010) 2090–2096, https://doi.org/10.1016/j.tsf.2009.08.011.
[13] S. Jeon, H. Lee, I. Jo, D. Shin, K.S. Lee, Degradation of TiN coatings on inconel 617 and silicon wafer substrates under pulsed laser ablation, J. Mater. Eng. Perform. 23 (2014) 1651–1655, https://doi.org/10.1007/s11665-014-0915-x.

[14] N. Seo, S. Jeon, Y. Choi, M.S. Jeon, H.G. Shin, H. Lee, Interfacial characteristics of TiN coatings on SUS304 and silicon wafer substrates with pulsed laser thermal shock, Korean J. Met. Mater 52 (2014) 81–85, https://doi.org/10.3365/Kjmm.2014.52.1.081.
[15] Y. Birol, D. Isler, Thermal cycling of AlTiN- and AlTiON-coated hot work tool steels at elevated temperatures, Mat Sci Eng a-Struct 528 (2011) 4703–4709, https://doi.org/10.1016/j.msea.2011.02.076.
[16] M. Nordin, R. Sundstrom, T.I. Selinder, S. Hogmark, Wear and failure mechanisms of multilayered PVD TiN/TaN coated tools when milling austenitic stainless steel, Surf. Coating. Technol. 133 (2000) 240–246, https://doi.org/10.1016/S0257-8972(00)00933-6.
[17] X. Chen, H.Q. Gao, Y.Y. Bai, H.S. Yang, Thermal failure mechanism of multilayer brittle TiN/CrAlN films, Ceram. Int. 44 (2018) 8138–8144, https://doi.org/10.1016/j.ceramint.2018.01.260.
[18] Q.S. Chen, C.H. Liu, R.Q. Zhang, H.Y. Yang, T.G. Wei, Y. Wang, Z. Li, L.X. He, J. Wang, L. Wang, J.P. Long, H. Chang, Microstructure and high-temperature steam oxidation properties of thick Cr coatings prepared by magnetron sputtering for accident tolerant fuel claddings: the role of bias in the deposition process, Corrosion Sci. 165 (2020), https://doi.org/10.1016/j.corsci.2019.108378.
[19] J. More-Chevalier, S. Cichoň, L. Horák, J. Bulíř, P. Hubík, Z. Gedeonová, L. Fekete, M. Poupon, J. Lančok, Correlation between crystallization and oxidation process of ScN films exposed to air, Appl. Surf. Sci. 515 (2020), https://doi.org/10.1016/j.apsusc.2020.145968.
[20] C. Meng, L. Yang, Y. Wu, J. Tan, W. Dang, X. He, X. Ma, Study of the oxidation behavior of CrN coating on Zr alloy in air, J. Nucl. Mater. 515 (2019) 354–369, https://doi.org/10.1016/j.jnucmat.2019.01.006.
[21] C.M.D. Starling, J.R.T. Branco, Thermal fatigue of hot work tool steel with hard coatings, Thin Solid Films 308 (1997) 436–442, https://doi.org/10.1016/S0040-6090(97)00600-7.
[22] H.M. Espejo, D.F. Bahr, Substrate cracking in Ti-6Al-4V driven by pulsed laser irradiation and oxidation, Surf. Coating. Technol. 322 (2017) 46–50, https://doi.org/10.1016/j.surfcoat.2017.05.001.
[23] M. Salem, S. Le Roux, G. Dour, P. Lamesle, K. Choquet, F. Rezai-Aria, Effect of aluminizing and oxidation on the thermal fatigue damage of hot work tool steels for high pressure die casting applications, Int. J. Fatig. 119 (2019) 126–138, https://doi.org/10.1016/j.ijfatigue.2018.09.018.
[24] Q.C. Jiang, X.M. Zhao, F. Qiu, T.N. Ma, Q.L. Zhao, The relationship between oxidation and thermal fatigue of martensitic hot-work die steels, Acta Metall Sin-Engl 31 (2018) 692–698, https://doi.org/10.1007/s40195-017-0699-8.
[25] Y. Birol, D. Isler, Response to thermal cycling of CAPVD (Al,Cr)N-coated hot work tool steel, Surf. Coating. Technol. 205 (2010) 275–280, https://doi.org/10.1016/j.surfcoat.2010.06.038.
[26] S. Jeon, B. Kim, Y. Choi, I. Jo, H. Lee, Thermal shock behaviors of Ti1-xZrxN coatings by accelerated test based on pulsed laser ablation, Ceram. Int. 42 (2016) 2241–2249, https://doi.org/10.1016/j.ceramint.2015.10.017.
[27] A. Horling, L. Hultman, M. Oden, J. Sjolen, L. Karlsson, Mechanical properties and machining performance of Ti1-xAlxN-coated cutting tools, Surf. Coating. Technol. 191 (2005) 384–392, https://doi.org/10.1016/j.surfcoat.2004.04.056.
[28] G. Skordaris, K.D. Bouzakis, P. Charalampous, E. Bouzakis, R. Paraskevopoulou, O. Lemmer, S. Bolz, Brittleness and fatigue effect of mono- and multi-layer PVD films on the cutting performance of coated cemented carbide inserts, CIRP Ann. -Manuf. Technol. 63 (2014) 93–96, https://doi.org/10.1016/j.cirp.2014.03.081.
[29] B. Zhao, X.X. Zhao, L.L. Lin, L.L. Zou, Effect of bias voltage on mechanical properties, milling performance and thermal crack propagation of cathodic arc ion -plated TiAlN coatings, Thin Solid Films (2020) 708, https://doi.org/10.1016/j.tsf.2020.138116. ARTN 138116.
[30] R. Daniel, J. Keckes, I. Matko, M. Burghammer, C. Mitterer, Origins of microstructure and stress gradients in nanocrystalline thin films: the role of growth parameters and self-organization, Acta Mater. 61 (2013) 6255–6266, https://doi.org/10.1016/j.actamat.2013.07.009.
[31] A.M. Engwall, Z. Rao, E. Chason, Origins of residual stress in thin films: interaction between microstructure and growth kinetics, Mater. Des. 110 (2016) 616–623, https://doi.org/10.1016/j.matdes.2016.07.089.
[32] M.T. Tilbrook, D.J. Paton, Z.H. Xie, M. Hoffman, Microstructural effects on indentation failure mechanisms in TiN coatings: finite element simulations, Acta Mater. 55 (2007) 2489–2501, https://doi.org/10.1016/j.actamat.2006.11.043.
[33] X.D. Sui, G.J. Li, X.S. Qin, H.D. Yu, X.K. Zhou, K. Wang, Q. Wang, Relationship of microstructure, mechanical properties and titanium cutting performance of TiAlN/TiAlSiN composite coated tool, Ceram. Int. 42 (2016) 7524–7532, https://doi.org/10.1016/j.ceramint.2016.01.159.
[34] F. Ahmed, K. Bayerlein, S.M. Rosiwal, M. Goken, K. Durst, Stress evolution and cracking of crystalline diamond thin films on ductile titanium substrate: Analysis by micro-Raman spectroscopy and analytical modelling, Acta Mater. 59 (2011) 5422–5433, https://doi.org/10.1016/j.actamat.2011.05.015.
[35] A. Le Febvrier, S. Deputier, V. Demange, V. Bouquet, A.C. Galca, A. Iuga, L. Pintilie, M. Guilloux-Viry, Effect of in-plane ordering on dielectric properties of highly {111}-oriented bismuth-zinc-niobate thin films, J. Mater. Sci. 52 (2017) 11306–11313, https://doi.org/10.1007/s10853-017-1297-x.
[36] C.H. Ma, J.H. Huang, H. Chen, Residual stress measurement in textured thin film by grazing-incidence X-ray diffraction, Thin Solid Films 418 (2002) 73–78, https://doi.org/10.1016/S0040-6090(02)00680-6. Pii S0040-6090(02)00680-6.
[37] G. Liu, Y. Yang, B. Huang, X. Luo, S. Ouyang, G. Zhao, N. Jin, P. Li, Effects of substrate temperature on the structure, residual stress and nanohardness of Ti6Al4V films prepared by magnetron sputtering, Appl, Surf. Sci. 370 (2016) 53–58, https://doi.org/10.1016/j.apsusc.2016.02.021.
[38] P. Eklund, N.J. Mikkelsen, M. Sillassen, E.J. Bienk, J. Bottiger, Chromium oxide-based multilayer coatings deposited by reactive magnetron sputtering in an industrial setup, Surf. Coating. Technol. 203 (2008) 156–159, https://doi.org/10.1016/j.surfcoat.2008.08.035.
[39] B. Peng, H. Li, Q. Zhang, Y.X. Xu, T. Wei, Q. Wang, F. Zhang, K.H. Kim, High-temperature thermal stability and oxidation resistance of Cr and Ta co-alloyed Ti − Al − N coatings deposited by cathodic arc evaporation, Corrosion Sci. 167 (2020), https://doi.org/10.1016/j.corsci.2020.108490.
[40] A. le Febvrier, N. Tureson, N. Stilkerich, G. Greczynski, P. Eklund, Effect of impurities on morphology, growth mode, and thermoelectric properties of (111) and (001) epitaxial-like ScN films, J. Phys. D Appl. Phys. 52 (2019), https://doi.org/10.1088/1361-6463/aaeb1b. ARTN 035302.
[41] N. Tureson, M. Marteau, T. Cabioch, N.V. Nong, J. Jensen, J. Lu, G. Greczynski, D. Fournier, N. Singh, A. Soni, L. Belliard, P. Eklund, A. le Febvrier, Effect of ion-implantation-induced defects and Mg dopants on the thermoelectric properties of ScN, Phys. Rev. B 98 (2018), https://doi.org/10.1103/PhysRevB.98.205307. ARTN 205307.
[42] J.A. Thornton, Influence of apparatus geometry and deposition conditions on the structure and topography of thick sputtered coatings, J. Vac. Sci. Technol. 11 (1974) 666–670, https://doi.org/10.1116/1.1312732.
[43] R. Daniel, K.J. Martinschitz, J. Keckes, C. Mitterer, The origin of stresses in magnetron-sputtered thin films with zone T structures, Acta Mater. 58 (2010) 2621–2633, https://doi.org/10.1016/j.actamat.2009.12.048.
[44] H. Liu, J.-F. Tang, X. Wang, W. Li, C.-L. Chang, Effects of nitrogen-argon flow ratio on the microstructural and mechanical properties of TiAlSiN/CrN multilayer coatings prepared using high power impulse magnetron sputtering, J. Vac. Sci. Technol., A 37 (2019), https://doi.org/10.1116/1.5100340.
[45] X. Zhang, Y. Duan, X. Dai, T. Li, Y. Xia, P. Zheng, H. Li, Y. Jiang, Atomistic origin of amorphous-structure-promoted oxidation of silicon, Appl. Surf. Sci. 504 (2020), https://doi.org/10.1016/j.apsusc.2019.144437.
[46] T. Kuznetsova, V. Lapitskaya, A. Khabarava, S. Chizhik, B. Warcholinski, A. Gilewicz, The influence of nitrogen on the morphology of ZrN coatings deposited by magnetron sputtering, Appl. Surf. Sci. 522 (2020), https://doi.org/10.1016/j.apsusc.2020.146508.
[47] J.-H. Huang, C.-H. Lin, G.-P. Yu, Texture evolution of vanadium nitride thin films, Thin Solid Films (2019) 688, https://doi.org/10.1016/j.tsf.2019.137415.
[48] F. Nita, C. Mastail, G. Abadias, Three-dimensional kinetic Monte Carlo simulations of cubic transition metal nitride thin film growth, Phys. Rev. B 93 (2016), https://doi.org/10.1103/PhysRevB.93.064107.
[49] F.F. Leal, S.C. Ferreira, S.O. Ferreira, Modelling of epitaxial film growth with an Ehrlich-Schwoebel barrier dependent on the step height, J Phys-Condens Mat 23 (2011), https://doi.org/10.1088/0953-8984/23/29/292201. Artn 292201.
[50] K. Balasubramanian, S.V. Khare, D. Gall, Energetics of point defects in rocksalt structure transition metal nitrides: thermodynamic reasons for deviations from stoichiometry, Acta Mater. 159 (2018) 77–88, https://doi.org/10.1016/j.actamat.2018.07.074.
[51] K.M. Calamba, J. Salamania, M.P.J. Jõesaar, L.J.S. Johnson, R. Boyd, J.F. Pierson, M.A. Sortica, D. Primetzhofer, M. Odén, Effect of nitrogen vacancies on the growth, dislocation structure, and decomposition of single crystal epitaxial (Ti1-xAlx)Ny thin films, Acta Mater. 203 (2021), https://doi.org/10.1016/j.actamat.2020.116509.
[52] A. le Febvrier, N.V. Nong, G. Abadias, P. Eklund, P-type Al-doped Cr-deficient CrN thin films for thermoelectrics, APEX 11 (2018). Artn 05100310.7567/Apex.11.051003.
[53] Y.T. Xi, K.W. Gao, X.L. Pang, H.S. Yang, X.T. Xiong, H. Li, A.A. Volinsky, Film thickness effect on texture and residual stress sign transition in sputtered TiN thin films, Ceram. Int. 43 (2017) 11992–11997, https://doi.org/10.1016/j.ceramint.2017.06.050.
[54] A. Jamnig, N. Pliatsikas, K. Sarakinos, G. Abadias, The effect of kinetics on intrinsic stress generation and evolution in sputter-deposited films at conditions of high atomic mobility, J. Appl. Phys. 127 (2020), https://doi.org/10.1063/1.5130148.
[55] M. Bartosik, D. Holec, D. Apel, M. Klaus, C. Genzel, J. Keckes, M. Arndt, P. Polcik, C.M. Koller, P.H. Mayrhofer, Thermal expansion of Ti-Al-N and Cr-Al-N coatings, Scripta Mater. 127 (2017) 182–185, https://doi.org/10.1016/j.scriptamat.2016.09.022.
[56] B.Q. Xu, L.R. Luo, J. Lu, X.F. Zhao, P. Xiao, Effect of residual stress on the spallation of the thermally-grown oxide formed on NiCoCrAlY coating, Surf. Coating. Technol. (2020) 381, https://doi.org/10.1016/j.surfcoat.2019.125112.
[57] P.H. Mayrhofer, F. Rovere, M. Moser, C. Strondl, R. Tietema, Thermally induced transitions of CrN thin films, Scripta Mater. 57 (2007) 249–252, https://doi.org/10.1016/j.scriptamat.2007.03.058.
[58] A. Lippitz, T. Hubert, XPS investigations of chromium nitride thin films, Surf. Coating. Technol. 200 (2005) 250–253, https://doi.org/10.1016/j.surfcoat.2005.02.091.
[59] O. Cortazar-Martínez, J.-A. Torres-Ochoa, J.-G. Raboño-Borbolla, A. Herrera-Gomez, Oxidation mechanism of metallic chromium at room temperature, Appl. Surf. Sci. 542 (2021), https://doi.org/10.1016/j.apsusc.2020.148636.
[60] A. Moatti, R. Bayati, J. Narayan, Epitaxial growth of rutile TiO2 thin films by oxidation of TiN/Si{100} heterostructure, Acta Mater. 103 (2016) 502–511, https://doi.org/10.1016/j.actamat.2015.10.022.
[61] Y.S. Kim, Y.H. Jeong, J.N. Jang, Stress measurements during thin film zirconium oxide growth, J. Nucl. Mater. 412 (2011) 217–220, https://doi.org/10.1016/j.jnucmat.2011.03.001.
[62] J.-C. Brachet, E. Rouesne, J. Ribis, T. Guilbert, S. Urvoy, G. Nony, C. Toffolon-Masclet, M. Le Saux, N. Chaabane, H. Palancher, A. David, J. Bischoff, J. Augereau, E. Pouillier, High temperature steam oxidation of chromium-coated zirconium-

based alloys: kinetics and process, Corrosion Sci. 167 (2020), https://doi.org/10.1016/j.corsci.2020.108537.
[63] J. Liu, Z. Cui, D. Ma, J. Lu, Y. Cui, C. Li, W. Liu, Z. Hao, P. Hu, M. Yao, P. Huang, G. Bai, D. Yun, Investigation of oxidation behaviors of coated Zircaloy as accident-tolerant fuel with CrAlN and CrAlSiN coatings in high-temperature steam, Corrosion Sci. 175 (2020), https://doi.org/10.1016/j.corsci.2020.108896.
[64] B.-S. Lou, Y.-C. Chang, J.-W. Lee, High temperature oxidation behaviors of CrNx and Cr-Si-N thin films at 1000 °C, Coatings (2019) 9, https://doi.org/10.3390/coatings9090540.
[65] B. Warcholinski, A. Gilewicz, P. Myslinski, E. Dobruchowska, D. Murzynski, Structure and properties of AlCrN coatings deposited using cathodic arc evaporation, Coatings (2020) 10, https://doi.org/10.3390/coatings10080793.
[66] B.D. Ozsdolay, C.P. Mulligan, K. Balasubramanian, L.P. Huang, S.V. Khare, D. Gall, Cubic beta-WNx layers: growth and properties vs N-to-W ratio, Surf. Coating. Technol. 304 (2016) 98–107, https://doi.org/10.1016/j.surfcoat.2016.06.079.
[67] B. Bouaouina, A. Besnard, S.E. Abaidia, A. Airoudj, F. Bensouici, Correlation between mechanical and microstructural properties of molybdenum nitride thin films deposited on silicon by reactive RF magnetron discharge, Surf. Coating. Technol. 333 (2018) 32–38, https://doi.org/10.1016/j.surfcoat.2017.10.028.
[68] H. Kindlund, D.G. Sangiovanni, J. Lu, J. Jensen, V. Chirita, J. Birch, I. Petrov, J. E. Greene, L. Hultman, Vacancy-induced toughening in hard single-crystal V 0.5 Mo 0.5 N x/MgO(0 0 1) thin films, Acta Mater. 77 (2014) 394–400, https://doi.org/10.1016/j.actamat.2014.06.025.